2013

# Divergent Eddy Heat Fluxes in the Kuroshio Extension at 144°–148°E. Part I: Mean Structure

Stuart P. Bishop

D. Randolph Watts
*University of Rhode Island*, randywatts@uri.edu

***See next page for additional authors***



Citation/Publisher Attribution

Bishop, S. P., Watts, D. R., & Donohue, K. A. (2013). Divergent Eddy Heat Fluxes in the Kuroshio Extension at 144°–148°E. Part I: Mean Structure. *J. Phys. Oceanogr., 43*, 1533-1550. doi: 10.1175/JPO-D-12-0221.1
Available at: http://dx.doi.org/10.1175/JPO-D-12-0221.1

# Divergent Eddy Heat Fluxes in the Kuroshio Extension at 144°–148°E. Part I: Mean Structure

STUART P. BISHOP

*National Center for Atmospheric Research, Boulder, Colorado*

D. RANDOLPH WATTS AND KATHLEEN A. DONOHUE

*Graduate School of Oceanography, University of Rhode Island, Narragansett, Rhode Island*

(Manuscript received 7 November 2012, in final form 3 May 2013)

ABSTRACT

The Kuroshio Extension System Study (KESS) provided 16 months of observations to quantify eddy heat flux (EHF) from a mesoscale-resolving array of current- and pressure-equipped inverted echo sounders (CPIES). The mapped EHF estimates agreed well with point in situ measurements from subsurface current meter moorings. Geostrophic currents determined with the CPIES separate the vertical structure into an equivalent-barotropic internal mode and a nearly depth-independent external mode measured in the deep ocean. As a useful by-product of this decomposition, the divergent EHF (DEHF) arises entirely from the correlation between the external mode and the upper-ocean thermal front. EHFs associated with the internal mode are completely rotational. DEHFs were mostly downgradient and strongest just upstream of a mean trough at ~147°E. The downgradient DEHFs resulted in a mean-to-eddy potential energy conversion rate that peaked midthermocline with a magnitude of $10 \times 10^{-3}\,\mathrm{cm^2\,s^{-3}}$ and a depth-averaged value of $3 \times 10^{-3}\,\mathrm{cm^2\,s^{-3}}$. DEHFs were vertically coherent, with subsurface maxima exceeding $400\,\mathrm{kW\,m^{-2}}$ near 400-m depth. The subsurface maximum DEHFs occurred near the depth where the quasigeostrophic potential vorticity lateral gradient changes sign from one layer to the next below it. The steering level is deeper than this depth of maximum DEHFs. A downgradient parameterization could be fitted to the DEHF vertical structure with a constant eddy diffusivity $\kappa$ that had values of $800–1400\,\mathrm{m^2\,s^{-1}}$ along the mean path. The resulting divergent meridional eddy heat transport across the KESS array was 0.05 PW near 35.25°N, which may account for ~1/3 of the total Pacific meridional heat transport at this latitude.

## 1. Introduction

Understanding the ocean's role in poleward heat transport $Q_v$ is pivotal to the climate problem. The best estimates using indirect methods show that $Q_v$ reaches a maximum between 20° and 30° in both the north and south hemispheres at 1.5–2 PW (PW = $10^{15}$ W), which is from about 1/4 to 1/3 of the total global meridional energy transport that peaks near 35° latitude of about 5.5–6 PW (Trenberth and Caron 2001). The principal uncertainty in estimating $Q_v$ from direct observations is due to mesoscale eddies, variability with time scales from weeks to months, and horizontal scales from tens to hundreds of kilometers. They are ubiquitous features in the ocean as observed from satellite altimetry (Ducet and Le-Traon 2001). Eddies drive a heat flux because of the temporal correlation $\overline{\mathbf{u}'T'}$ between $T'$ temperature and $\mathbf{u}'$ velocity fluctuations, where a bar indicates a time mean and a prime a deviation from the time mean.

The role that eddies play in ocean stirring and driving circulation is poorly understood due in large part to the sparseness of observations and inadequate current and temperature record lengths for reliable statistical estimates. Moreover large vector rotational components in the $\overline{\mathbf{u}'T'}$ field that play no role in net heat exchange mask the dynamically important divergent fluxes, making sparse observations difficult to interpret.

Current global climate models are unable to resolve mesoscale eddies and are reliant upon advective parameterizations (Gent and McWilliams 1990), but whether they are correct is unclear. Available observations and eddy-permitting models point to the western

*Corresponding author address:* Stuart P. Bishop, National Center for Atmospheric Research, P.O. Box 3000, Boulder, CO 80307.
E-mail: sbishop@ucar.edu

DOI: 10.1175/JPO-D-12-0221.1

boundary current (WBC) extensions and the Antarctic Circumpolar Current (ACC) as having significant poleward eddy heat transport contributing to the total heat transport (Wunsch 1999; Jayne and Marotzke 2002; Volkov et al. 2008). Within the ocean interior away from lateral and vertical boundary layers, eddies are the primary means by which heat is transported poleward in WBC extensions and the ACC. These intense primarily zonal frontal boundaries act as barriers to cross-frontal exchange. Meanders presumably induced by instabilities and mesoscale eddy interaction are the processes that allow cross-frontal heat exchange.

WBC extensions and the ACC exhibit longitudinal variability in eddy–mean flow interactions. From an idealized modeling study with parameters similar to the Kuroshio Extension, Waterman and Jayne (2011) found that a stabilization point exists in the downstream development of WBC jets. Upstream of this stabilization point, eddies act to take energy from the background-mean state and vice versa downstream. There is some evidence of this type of structure in the Gulf Stream (Cronin and Watts 1996; Bower and Hogg 1996) and Kuroshio Extension (Waterman et al. 2011; Hall 1991) from observations that show a transition from an eddy-growing to eddy-decaying region in the downstream direction. These observations are sparse, however, and whether a stabilization point exists is inconclusive.

Attempts have been made to estimate eddy heat flux (EHF) from observations in the Kuroshio Extension (Qiu and Chen 2005a), Gulf Stream (Cronin and Watts 1996; Dewar and Bane 1989; Rossby 1987; Hall 1986), and the Southern Ocean (Walkden et al. 2008; Phillips and Rintoul 2000; Bryden 1979). With the exception of Cronin and Watts (1996), none of these studies have made the distinction between divergent and rotational EHF. It is the divergent EHF (DEHF) that is responsible for driving net heat transport. Marshall and Shutts (1981) developed a method in which a large rotational component of the EHF can be projected onto temperature variance contours. The residual component contains the divergence and this method has been used in the analysis of atmosphere (Illari and Marshall 1983; Shutts 1986) and ocean (Cronin and Watts 1996; Cronin 1996) observations.

Until recently, moored observations in the Gulf Stream far outnumbered those in the Kuroshio Extension. Questions remain concerning how mesoscale eddies influence the Kuroshio Extension–mean flow and how the different topography and stratification of the Kuroshio Extension system influence the spatial structure of eddy fluxes. The Kuroshio Extension System Study (KESS), a multi-institutional effort to understand the mesoscale variability of the jet, addressed these questions. The observational network comprised 46 current- and pressure-equipped inverted echo sounders (CPIES) and eight subsurface moorings. These were deployed for 2 years from June 2004 to July 2006 to the east of Japan in the region of highest eddy kinetic energy (EKE) (Fig. 1).

The KESS observational field study captured a diverse range of mesoscale phenomena: upper-baroclinic frontal meanders ranging from 6- to 40-day variability (Tracey et al. 2012); nearly depth-independent deep eddies in the 30–60-day band that were generated external to the KESS array and propagated from the northeast into the region where they coupled with upper-baroclinic meanders (Greene 2010; Tracey et al. 2012); cold-core ring (CCR) formation; and warm- and cold-core ring–jet interaction. The KESS observations also fortuitously captured a regime shift from a weakly meandering (stable) regime to a strongly meandering (unstable) regime, which varies on decadal time scales as shown by Qiu and Chen (2005b).

This study uses the first 16 months of KESS observations to quantify the mean structure of DEHFs and their role in eddy–mean flow energy conversion between 144° and 148°E. A companion paper presents the spatiotemporal variability of the DEHFs. Eddy forcing by eddy heat fluxes, as in the transformed Eulerian mean in Cronin (1996) is dealt with in chapter 3 of Bishop (2012) and is a manuscript in preparation. The paper is organized as follows. In section 2, a description of the instrumentation is given. In section 3, the EHFs from the subsurface moorings are quantified using standard methods, that is, Phillips and Rintoul (2000), without making distinctions between divergent and rotational fluxes. Section 4 compares the CPIES-mapped estimates of EHF with those made from point estimates at the subsurface moorings. Section 5 describes the CPIES-mapped EHF and distinguishes between divergent and rotational fluxes. Section 6 shows the mean spatial structure of the DEHFs with an emphasis on mean-to-eddy energy conversion. In section 7, the EHF is vertically and zonally integrated to estimate eddy heat transport. The final section presents the discussion and conclusions.

## 2. Data

### *a. Current meter moorings*

Seven current meter moorings (K1–K7) were deployed for 2 years during KESS with an eighth mooring (K8) deployed during the second year (Fig. 1). The moorings were located between the first quasi-stationary meander crest and trough to the east of Japan in the region of highest EKE. They spanned the Kuroshio

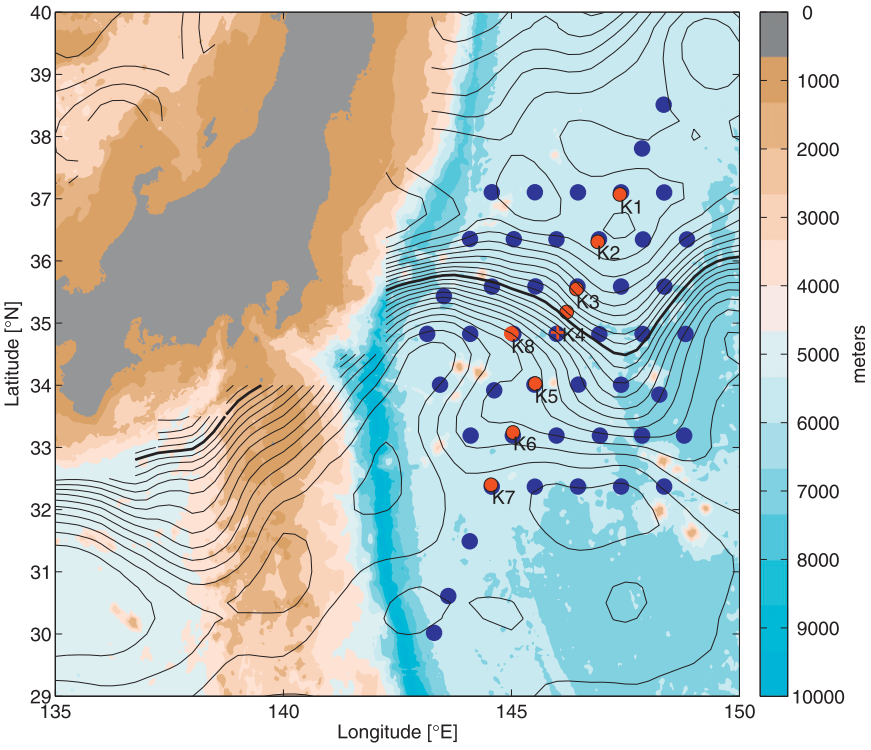


FIG. 1. KESS observing array. Blue circles are the locations of CPIES and red circles are the locations of the subsurface moorings. The red cross is the location of subsurface mooring K4 during the second year. Color shades indicate ocean bathymetry from Smith and Sandwell (1997). Black contours are the mean sea surface height (SSH) contours [contour interval (CI) = 0.05 m] from the satellite altimetry Archiving, Validation, and Interpretation of Satellite Oceanographic data (AVISO) product with RIO05 mean dynamic topography over the duration of the KESS experiment (June 2004–July 2006). The thick black contour is representative of the jet axis (2.1-m SSH contour).

Extension from north to south, and were collocated with a *Jason-1* altimeter line.

The moorings were equipped with an upward-looking acoustic Doppler current profiler (ADCP) at 250 m; a McLane Moored Profiler (MMP), which traveled between 250- and 1500-m depth; a vector-averaging current meter (VACM) at 1500 m; and Aanderaa RCM11 acoustic current meters at 2000, 3500, and 5000 m. An additional VACM was deployed for one year at 250 m at K4 and K5 for the first year and K8 for the second year.

The VACMs and RCM11s had >80% data return (Jayne et al. 2009), but the MMPs incurred many data losses. The MMPs were designed to measure temperature, conductivity, and current velocity while completing a roundtrip from 250 to 1500 m every 15 h. The MMPs tended to stop working during strong current events, which resulted in spotty records. The MMPs will only be used here for comparing between in situ and simultaneous CPIES estimates of EHFs.

The VACMs and RCM11s measured temperature and current velocity. The data were twice-daily averaged and 3-day low-pass filtered using a fourth-order Butterworth filter to remove tidal influences. In addition, the RCM11 current speeds were corrected for the speed of sound and adjusted upward by 10% because Hogg and Frye (2007) found that the currents tended to be biased low when compared with other current meters.

### *b. CPIES*

Forty-six CPIES were deployed in a ~600 km × 600 km array spanning the Kuroshio Extension jet for 2 years during KESS (Fig. 1). At three sites collocated with moored current meters, the CPIES were replaced with PIES. The CPIES array was centered in the region of highest surface EKE from satellite altimetry (143°–149°E) and spanned the meander envelope from north to south, capturing almost one full wavelength of the quasi-stationary meander crest-trough-crest to the east of Japan (Mizuno and White 1983). The CPIES array had a nominal horizontal spacing of 88 km, to resolve mesoscale variability. Of the CPIES, 26 were collocated

with *Jason-1* altimetry lines for comparative studies (Park et al. 2012; Bishop et al. 2012).

The CPIES array maps the geostrophic current and density field throughout the water column. The processing of the CPIES to map density and absolute geostrophic currents is documented in Donohue et al. (2010) and will be briefly summarized here. The CPIES measures the following: round-trip acoustic travel time $\tau$ of a 12-kHz pulse from the sea floor to the sea surface using the inverted echo sounder; currents at 50 m off the bottom from an Aanderaa RCM-11 head; and bottom pressure using a Paroscientific Digiquartz pressure sensor located within the inverted echo sounder housing.

A lookup table between $\tau$, integrated from the surface to a reference depth, and hydrographic properties yielded vertical profiles of temperature and density at each CPIES site. The lookup table was created from empirical relationships established with historical hydrography known as the gravest empirical mode (GEM) method (Watts et al. 2001b; Meinen and Watts 1998). The GEM method provides time series profiles of geopotential $\Phi$.

Geostrophic currents determined from the CPIES separate the vertical structure into an equivalent-barotropic internal mode $\mathbf{u}_I$ and a nearly depth-independent external mode $\mathbf{u}_E$. Equivalent barotropic means that the flow is vertically aligned (no turning with depth), but the amplitude of the current varies with depth. Equivalent barotropicity is a good approximation for the Kuroshio Extension and other strong current systems such as the ACC (Killworth 1992).

The internal mode geostrophic current profiles, in thermal wind balance, were estimated from the baroclinicity of the current by the mapped geopotential as a function of pressure

$$f\mathbf{u}_I = \mathbf{k} \times \nabla\Phi, \tag{1}$$

referenced to 5300 dbar, where $f$ is the Coriolis parameter, $\mathbf{k}$ is the vertical unit vector aligned with the gravitational acceleration, and $\nabla = (\partial/\partial x, \partial/\partial y)$ is the horizontal gradient operator. Measurements from the current meters and pressure gauges at the bottom provided the external mode and reference current at 5300 dbar $\mathbf{u}_E$ that is nearly depth independent away from steep topography (Bishop et al. 2012) to establish absolute geostrophic current profiles

$$\mathbf{u} = \mathbf{u}_I + \mathbf{u}_E. \tag{2}$$

The geostrophic streamfunction $\psi$ defined from the nondivergent field $\nabla \cdot (f\mathbf{u}) = 0$ is equivalent to geopotential $\psi = \Phi$, where the dependence of $f$ upon latitude is necessarily included because of the meridional extent of the KESS array.

The KESS array provided full maps of current and temperature for 16 months from June 2004 to September 2005, after which some CPIES stopped working early. The CPIES were twice-daily averaged and 3-day low-pass filtered using a fourth-order Butterworth filter to remove tidal influences. Additional subregions can be mapped until April 2006. The temperature and current maps agree very well compared to point measurements from the current meter moorings (Donohue et al. 2010).

## 3. Traditional eddy heat fluxes

Traditional estimates of the statistical correlation between temperature and currents were made from point measurements at the current meter moorings to calculate EHF, making no distinction between divergent and rotational fluxes. The calculations are traditional in the sense that before large observational arrays were deployed, oceanographers made and still do make estimates of EHF from isolated current meter moorings. Here, to present context for comparison with historical efforts, the traditional estimates of EHF are reported for the KESS subsurface moorings.

EHF estimates $\rho_0 C_p \overline{\mathbf{u}'T'}$ were made using all available current meter data. The density and specific heat used for these calculations was the depth-averaged density over the region: $\rho_0 = 1027.5\,\mathrm{kg\,m^{-3}}$ and $C_p = 4000\,\mathrm{J\,kg^{-1}\,°C^{-1}}$, respectively. EHF has units of watts per square meter and in the literature is commonly reported in units of kilowatts per square meter. The estimates were made at 250, 1500, 2000, 3500, and 5000 m. No common time was used for these statistical estimates. Instead, estimates were made for each site based on the time interval of good data from each individual instrument (time intervals listed in Table 1).

### a. Mooring motion correction

Mooring motion correction is important because of drawdown of moorings when current drag is strong introduces variations $T'$ in the measured temperatures. The temperature variations are unavoidably correlated with the velocity variations $\mathbf{u}'$ (Hogg 1986), producing $\overline{\mathbf{u}'T'}$ correlations that are large and difficult to separate from those resulting from the heat flux. For example, the current meters at 250 dbar were drawn down as much as 400 dbar (Fig. 2a). The rms deflections from 250 dbar at sites K4, K5, and K8 were 138, 101, and 135 dbar, respectively. It has been suggested that temperature corrections for mooring motion can be made more accurately using a GEM lookup table (Meinen 2008) than by other methods that assume "parallel isotherms" across a front (e.g., Hogg 1986). To correct for these defects, the current meters at 250 and 1500 m, which had

TABLE 1. EHF estimates ($kW\,m^{-2}$) for KESS moorings. Here, * and ** indicate sites that had significant correlations at 95% and 90% confidence, respectively. Sites at 250 and 1500 dbar were corrected for mooring motion except for K8 at 1500 dbar which did not have a pressure record.

| Site | Depth (dbar) | $\rho_0 C_p \overline{u'T'}$ | $\rho_0 C_p \overline{v'T'}$ | Time interval |
|---|---|---|---|---|
| K1 | 2000 | −1.17 | −1.95 | 8 Jun 2005–18 May 2006 |
| | 5000 | 0.04 | −0.09 | 8 Jun 2004–15 May 2006 |
| K2 | 1500 | 3.20 | −2.79 | 9 Jun 2004–19 May 2006 |
| | 2000 | −0.07 | **−2.27 | 9 Jun 2004–5 Dec 2005 |
| | 3500 | 0.09 | *−0.53 | 9 Jun 2004–19 May 2006 |
| | 5000 | −0.01 | −0.08 | 9 Jun 2004–29 Dec 2005 |
| K3 | 1500 | *16.81 | −7.41 | 10 Jun 2004–20 May 2006 |
| | 2000 | *6.30 | −3.38 | 10 Jun 2004–20 May 2006 |
| | 3500 | *1.60 | 0.26 | 10 Jun 2004–7 Feb 2006 |
| | 5000 | *0.57 | 0.45 | 10 Jun 2004–1 Nov 2005 |
| K4 | 250 | −104.97 | −2345.60 | 14 Jun 2004–1 Jun 2005 |
| | 1500 | −1.63 | 2.44 | 9 Jun 2005–21 May 2006 |
| | 2000 | 4.48 | 2.29 | 14 Jun 2004–21 May 2006 |
| | 3500 | *1.74 | 0.67 | 14 Jun 2004–13 Mar 2006 |
| | 5000 | *0.46 | 0.21 | 14 Jun 2004–8 Feb 2006 |
| K8 | 250 | *2378.80 | −1279.30 | 13 Jun 2005–25 Apr 2006 |
| | 1500 | *8.63 | 11.30 | 14 Jun 2005–21 May 2006 |
| | 2000 | *7.33 | 3.51 | 14 Jun 2005–21 May 2006 |
| | 3500 | *1.50 | 0.20 | 14 Jun 2005–21 May 2006 |
| | 5000 | *0.35 | −0.10 | 14 Jun 2005–21 May 2006 |
| K5 | 250 | *1516.40 | *−434.50 | 15 Jun 2004–7 Jun 2005 |
| | 1500 | *26.69 | *−21.98 | 15 Jun 2004–22 May 2006 |
| | 2000 | *8.69 | −8.55 | 15 Jun 2004–22 May 2006 |
| | 3500 | *1.12 | −0.23 | 15 Jun 2004–9 Mar 2006 |
| | 5000 | *0.32 | 0.08 | 15 Jun 2004–17 May 2006 |
| K6 | 1500 | −6.80 | −0.01 | 15 Jun 2004–22 May 2006 |
| | 2000 | −0.60 | 1.17 | 15 Jun 2004–22 May 2006 |
| | 3500 | *0.90 | −0.61 | 15 Jun 2004–6 Mar 2006 |
| | 5000 | −0.35 | 0.53 | 16 Jun 2004–10 May 2006 |
| K7 | 1500 | −4.02 | **−7.85 | 16 Jun 2004–23 May 2006 |
| | 2000 | −4.64 | **−3.86 | 16 Jun 2004–23 May 2006 |
| | 3500 | 0.47 | 0.14 | 16 Jun 2004–21 Jan 2006 |
| | 5000 | −0.07 | 0.03 | 31 May 2005–22 Apr 2006 |

pressure records, were corrected for mooring motion and leveled to nominal depths of 250 and 1500 m, respectively, by the following technique. The correction was the difference between the CPIES-mapped estimate of temperature $T^p_{\mathrm{CPIES}}$ and current $\mathbf{u}^p_{\mathrm{CPIES}}$ at $p$ = 250 and 1500 dbar and the pressure of the current meter $p_{\mathrm{CM}}(t)$

$$\delta T(t) = T_{\mathrm{CPIES}}(p,t) - T_{\mathrm{CPIES}}[p_{\mathrm{CM}}(t),t] \quad \text{and} \quad (3)$$

$$\delta \mathbf{u}(t) = \mathbf{u}_{\mathrm{CPIES}}(p,t) - \mathbf{u}_{\mathrm{CPIES}}[p_{\mathrm{CM}}(t),t]. \quad (4)$$

These relatively small corrections were added to the current meter data

$$\mathbf{u}^p_{\mathrm{CM}}(t) = \mathbf{u}_{\mathrm{CM}}(p,t) + \delta \mathbf{u}(t) \quad \text{and} \quad (5)$$

$$T^p_{\mathrm{CM}} = T_{\mathrm{CM}}(p,t) + \delta T(t). \quad (6)$$

An example of the mooring motion correction for mooring K4 at the VACM at 250-m depth is shown in Fig. 2. The rms differences between the corrected and uncorrected current meter measurements were 13.2 and 9.76 $cm\,s^{-1}$ for the zonal and meridional currents, respectively, and 2.63°C for temperature, which are only 12%–15% of the observed range of measurements. Mooring motion corrections were not applied to current meters at 2000, 3500, and 5000 m because $p_{\mathrm{CM}}(t)$ was not measured.

### b. Results

A summary of the results can be found in Table 1. From Table 1, EHFs have largest magnitude in the upper ocean and near the mean path of the Kuroshio Extension at moorings K4, K5, and K8. The meridional components at 250 m are all negative at these sites reaching a maximum at K4 of $-2345.6\,kW\,m^{-2}$. These are 1-yr estimates at 250 m, during the first year of deployment at K4 and K5 and at K8 in the second year. The EHFs at 250 m are so strong because of the large rotational components, which mask the divergent component as will be discussed in a later section of this paper.

The subthermocline EHF estimates at 1500 m and deeper were better represented temporally, having almost 2 years of data. Figures 3a and 3b show the latitudinal dependence of the subthermocline EHFs. These point measurements will be discussed later in the context of the full-mapped EHFs. The zonal EHFs were mostly positive reaching values in excess of $20\,kW\,m^{-2}$ at 1500 m near 34°N. The meridional EHFs had similar magnitudes to the zonal component and were mostly negative, except near the mean path of the current at 35°N. Figure 3c shows that the EHF vectors at ~35°N had the only positive components down the mean temperature gradient near the mean path.

The magnitudes of these estimates made from the KESS observations are comparable to those at other strong current systems. In the Gulf Stream, meridional estimates were 7.6 $cm\,s^{-1}$ °C (312 $kW\,m^{-2}$) at 300-m depth at 73°W (Dewar and Bane 1989); 1.547, 3.901, and 0.055 $cm\,s^{-1}$ °C (64, 160, and 2.3 $kW\,m^{-2}$) at 575-, 875-, and 1175-m depth at 68°W (Hall 1986); and as large as $O$[100, 50, 10, and 1 $cm\,s^{-1}$ °C (4000, 2000, 400, 40 $kW\,m^{-2}$)] at 400-, 700-, 1000-, and 3500-m depth upstream of the standing meander trough axis at 68°W (Cronin and Watts 1996), where the values in parentheses

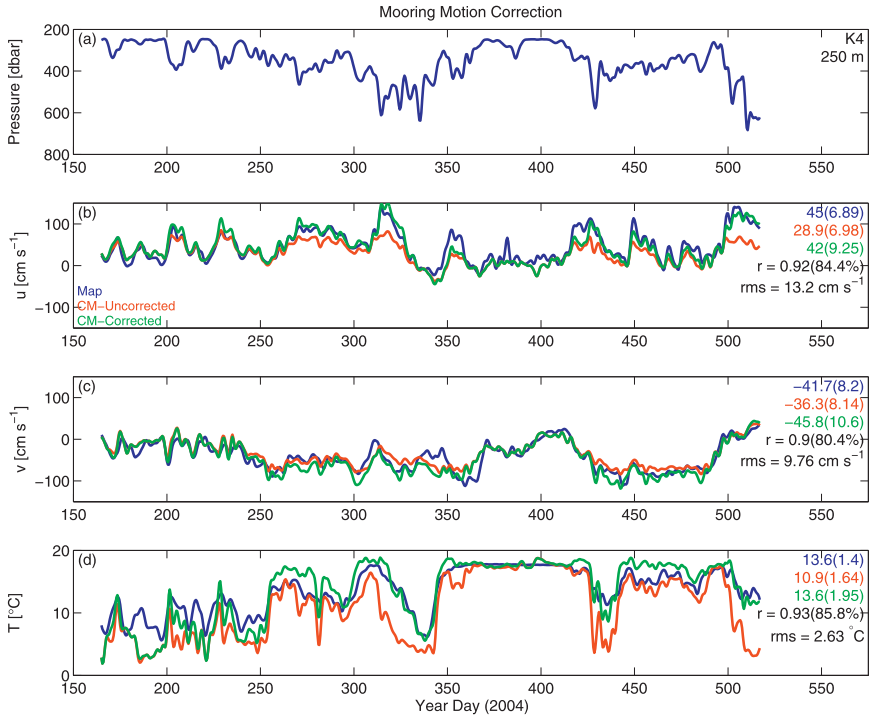


FIG. 2. Mooring motion correction for the VACM measurements at 250-m depth from mooring K4. (a) The pressure record, (b) the zonal current, (c) the meridional current, and (d) the temperature are shown. In (b)–(d), blue is the mapped estimate at 250 m, red is the uncorrected current meter measurement, and green is the corrected current meter measurement. In (b)–(d), the mean values for each color are shown with the standard error of the mean in parentheses, which takes into account effective degrees of freedom for correlated data by the autocorrelation function (Emery and Thomson 2001), $r$ is the correlation coefficient between the corrected current meter measurements and the mapped estimates with the percent of the variance in parentheses, and rms is the rms difference between the corrected and uncorrected current meter measurements.

were converted to kilowatts per square meter. In the Southern Ocean, the average poleward eddy heat flux is $6.7\,\mathrm{kW\,m^{-2}}$ at 2700 m in the Drake Passage (Bryden 1979), $14.0 \pm 5.7\,\mathrm{kW\,m^{-2}}$ at 2750 m at Shag Rocks Passage (Walkden et al. 2008), and the vertically averaged poleward eddy heat flux bandpass filtered (<90 days) is $11.3\,\mathrm{kW\,m^{-2}}$ to the south of Tasmania (Phillips and Rintoul 2000).

## 4. Comparisons between moorings and maps

This section will show that the mapped estimates of EHF from the CPIES array agree well with those made at the moorings. EHFs are the sum of a component associated with the internal mode currents [Eq. (1)] and a component associated with the deep reference currents [Eq. (2)]

$$\overline{\mathbf{u}'T'} = \overline{\mathbf{u}'_I T'} + \overline{\mathbf{u}'_E T'}. \qquad (7)$$

The mapped estimates of EHF from the CPIES array agree well with those made at the moorings. The focus of these comparisons is on the upper-ocean meridional component for sites near the mean jet path. This is done by comparing the time series of EHF from the VACMs at 250 m and the CPIES-mapped estimates at each respective location. Comparisons between time-mean estimates from the MMPs and the CPIES maps at the locations of the moorings, during times when they both worked simultaneously, also provide comparisons within the thermocline, where EHFs were expected to be strongest.

We used the most direct comparison between time series of EHF by following the time-varying pressure that was measured on the VACMs. The moorings were drawn down as much as 600 dbar. We sought to avoid introducing to this comparison the uncertainties of making corrections for the mooring motion. Hence, the mapped currents and temperature from CPIES were determined as a function of time at the same pressure as

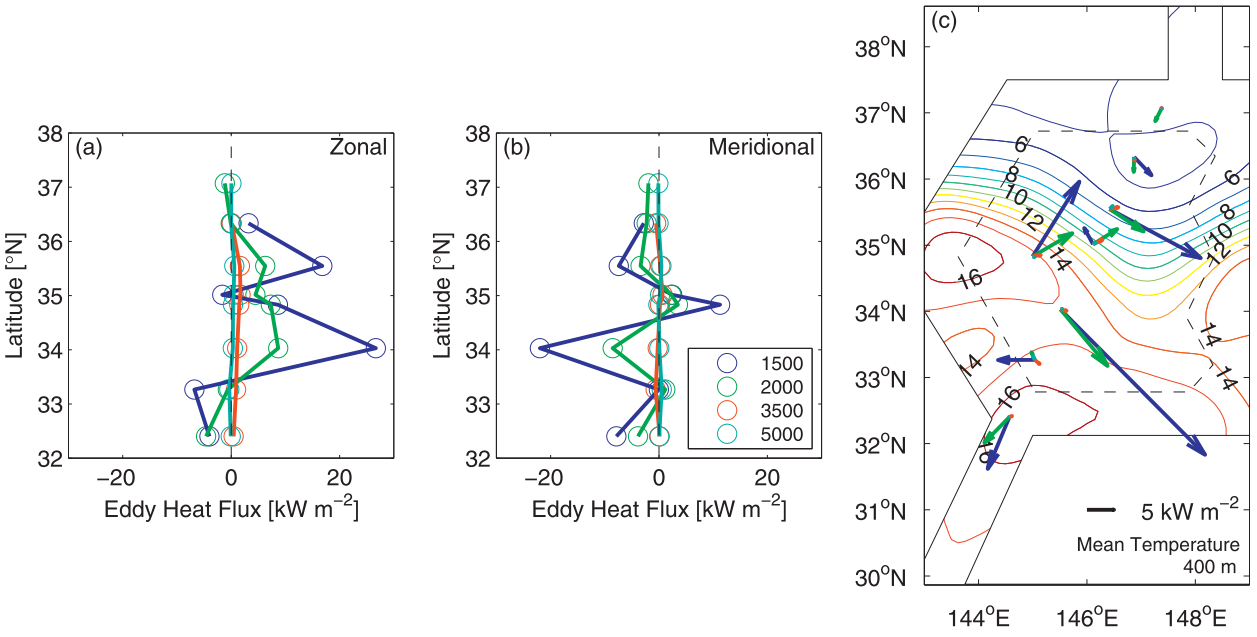


FIG. 3. Mean EHF for the subthermocline ocean from the current meter moorings. (a) Latitudinal dependence of the zonal EHF. (b) Latitudinal dependence of the meridional EHF. (c) EHF vectors superimposed on the mean temperature contours at 400 m mapped from the CPIES data. The region within the dashed line, which has the smallest error for gradient operations, will be the region of focus throughout the remaining paper.

the VACM measurements. This technique skirted any mooring motion correction scheme and provided the most direct way to compare the time series.

Time series comparisons at moorings sites K4, K5, and K8 are shown in Figs. 4a–c. The CPIES-mapped time series agree well with the current meter estimates. The two time series follow each other in time, capturing the same events, with correlation coefficients between the maps and moorings ranging from 0.74 to 0.94. The rms differences between the maps and moorings range from $21 \times 10^2$ to $42 \times 10^2$ kW m$^{-2}$, which is only 10%–20% of the $\pm 200 \times 10^2$ kW m$^{-2}$ range observed.

The MMPs provided current and temperature records through the thermocline from 250 to 1500 m, but as mentioned above stalled during strong events. Even though the MMP records had many data gaps, the time-mean and standard error of the mean (SEM) eddy heat flux was calculated for depths between 250 and 1000 m. For comparison, the time-mean EHF and standard error of the mean from the CPIES maps at the depths and locations of the moorings were calculated for coincident times when the MMPs were working.

The EHF profiles for sites spanning the mean jet path at K3, K4, and K5 are compared in Figs. 4d–f. At all the sites, the time-mean meridional EHF estimates agree in sign and magnitude. The mean values are statistically not different between 250 and 1000 dbar for K4 and K5 based on the standard error of the mean determined by the effective degrees of freedom for correlated times series (Emery and Thomson 2001). At K3, the CPIES-mean values were weaker in magnitude.

## 5. Mapped eddy heat fluxes

### *a. Theoretical background*

The results from the comparisons at the mooring sites in the previous section show that the CPIES maps give robust estimates of EHF. The remainder of this paper diagnoses EHF throughout the region mapped by CPIES. In particular, EHF can be quantified from the CPIES-mapped field of current and temperature throughout the water column. It is important to determine what dynamical role each component of the EHF plays in Eq. (7). A brief overview of the theoretical background on EHF is first presented to illustrate the dynamical role of divergent and rotational fluxes.

The mesoscale variability of the Kuroshio Extension can be examined in a quasigeostrophic (QG) framework because Rossby numbers (Ro) are small below 200 m (Howe et al. 2009). Within this theoretical framework, the Boussinesq, incompressible, and QG steady-state $O$(Ro) temperature equation in Cartesian coordinates is

$$\overline{\mathbf{u}} \cdot \nabla \overline{T} = -\overline{w}\Theta_z - \nabla \cdot \overline{\mathbf{u}'T'}, \qquad (8)$$

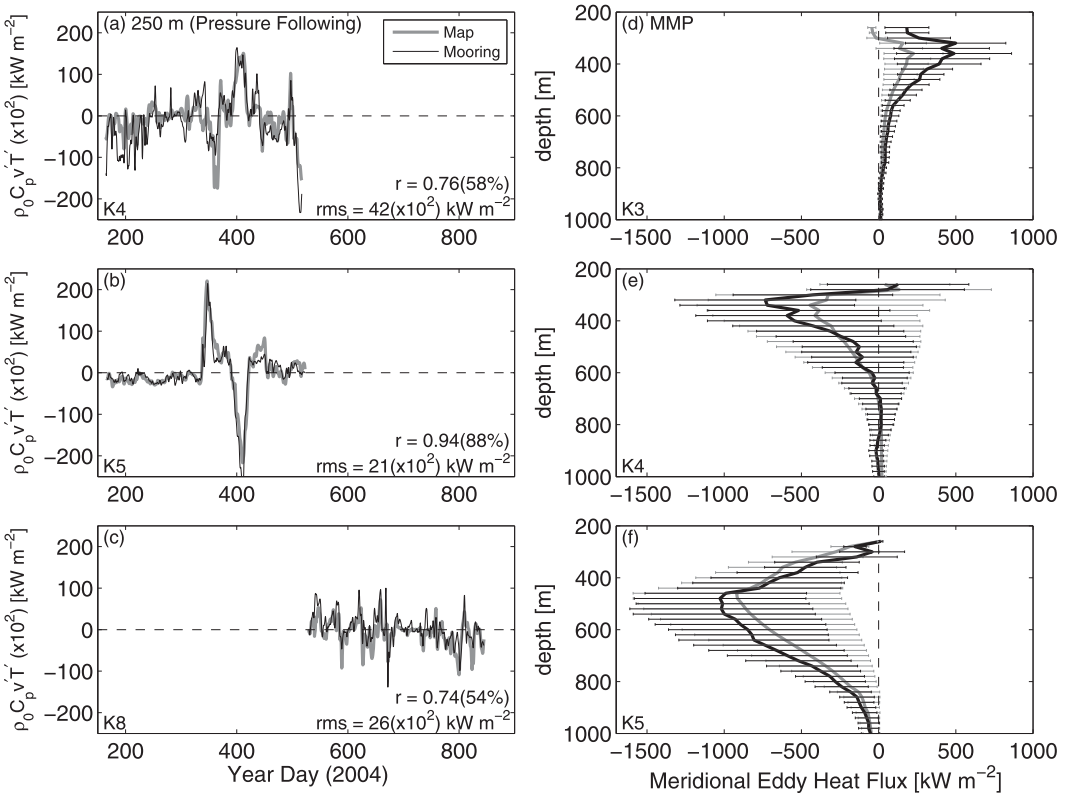


FIG. 4. Meridional EHF comparisons between CPIES maps (gray) and moorings (black). (a)–(c) Time series comparisons for sites K4, K5, and K8 from the VACM at 250 m, following the pressure record in time. (d)–(f) Time-mean meridional EHF for sites K3, K4, and K5 with SEM error bars for times when the MMPs were working, excising data from gaps in the record. Caution, these values should only be considered for comparison. Because the MMPs did not work during strong events, these mean values are not representative of the true mean and are likely an underestimate.

where $\mathbf{u} = (u, v)$ are the geostrophic currents in the zonal and meridional directions, respectively, $T$ is the temperature, $w$ is the vertical velocity, $\Theta(z)$ is the depth-dependent regional background potential temperature, subscript $z$ indicates a vertical derivative, overbar indicates a time mean, and prime indicates a deviation from the time mean. It is shown in Bishop (2012) that the balance of Eq. (8) generally holds with a small residual within the thermocline when the terms are zonally averaged. From the temperature equation [Eq. (8)], it is evident that mean temperature advection $\overline{\mathbf{u}} \cdot \nabla \overline{T}$ is balanced by mean vertical motion and the divergence of EHF. For the remainder of the paper, multiplication by $\rho_0$ (i.e., the depth-averaged density) and $C_p$ (i.e., the specific heat at constant pressure) will be implied for $\overline{\mathbf{u}'T'}$.

The divergent component of the EHF plays a dynamic role by advecting heat across a front to actively lower the available potential energy in a baroclinically unstable jet as seen from

$$\mathbf{u}' \cdot \nabla T' = \nabla \cdot \mathbf{u}' T', \tag{9}$$

where $\mathbf{u}'$ is nondivergent to $O(\beta U/f) = 10^{-7}\,\mathrm{s}^{-1}$, where $\beta = 2 \times 10^{-11}\,\mathrm{m}^{-1}\,\mathrm{s}^{-1}$, $U = O(1\,\mathrm{m\,s}^{-1})$ is a characteristic velocity scale, and $f = O(10^{-4}\,\mathrm{s}^{-1})$. Eddies that have a cross-isotherm component of the eddy velocity are responsible for driving divergent fluxes. Because the flow field for large-scale circulation is to first order geostrophic and nondivergent, nondivergent EHFs generally dominate over small divergent components that arise from advection of the temperature field. The EHF can be decomposed into purely divergent and rotational (nondivergent) components by Helmholtz's theorem,

$$\overline{\mathbf{u}'T'} = \overline{\mathbf{u}'T'}^{\mathrm{div}} + \overline{\mathbf{u}'T'}^{\mathrm{rot}}. \tag{10}$$

From this decomposition, one might seek to solve for the divergent component by solving Poisson's equation for a scalar potential $\nabla^2\phi = \epsilon$, with appropriate boundary conditions. Choosing the appropriate boundary conditions is a difficult problem and Fox-Kemper et al. (2003) argue that a unique solution for the divergent component of eddy flux may not exist in the presence of

boundaries. Particularly for KESS, which has open boundaries, it is not obvious what the boundary conditions should be.

A unique method, developed by Marshall and Shutts (1981, hereafter referred to as MS), estimates the divergent component of EHF for application to the eddy potential energy (EPE) equation. The steady-state temperature variance $\overline{T'^2}$ equation

$$\overline{\mathbf{u}} \cdot \nabla \frac{1}{2}\overline{T'^2} + \overline{\mathbf{u}'T'} \cdot \nabla \overline{T} + \overline{w'T'}\Theta_z = 0 \tag{11}$$

is the EPE equation when scaled by $\alpha g/\Theta_z$, where $\alpha$ is an effective thermal expansion coefficient on the order of $10^{-4}\,^{\circ}\mathrm{C}^{-1}$ for seawater, and $g$ is the acceleration as a result of gravity (Cronin and Watts 1996). EPE is defined as

$$\mathrm{EPE} = \frac{\alpha g}{2\Theta_z}\overline{T'^2}. \tag{12}$$

EPE, when multiplied by density, is expressed as an energy density with units of joules per cubic meter. It is conventional to divide by density and express EPE in units of joules per kilogram, which is equivalent to square meters per second squared. EPE and EKE, where $\mathrm{EKE} = 1/2(\overline{u'^2 + v'^2})$, are commonly reported in the literature in units of square centimeters per second squared, which is $10^4$ times greater than square meters per second squared. The energy conversion rates are then conventionally expressed in units of square centimeters per second cubed. Note that the triple correlation term $\nabla \cdot 1/2(\overline{\mathbf{u}'T'^2})$ was ignored in Eq. (11) and assumed to be small. Therefore, the MS method does not include contributions from the triple correlation term.

MS argue that, if the mean flow is approximately along mean temperature contours $\overline{\mathbf{u}} \cdot \nabla \overline{T} \approx 0$, then the mean streamfunction for the flow must be a function of the mean temperature $\overline{\psi} = \overline{\psi}(\overline{T})$. From this result, it can be shown that the cross-isotherm rotational EHFs balance the mean advection of EPE in Eq. (11)

$$\overline{\mathbf{u}} \cdot \nabla \frac{1}{2}\overline{T'^2} + \overline{\mathbf{u}'T'}^{\mathrm{rot}} \cdot \nabla \overline{T} = 0, \tag{13}$$

where the rotational EHF is related to the temperature variance by

$$\overline{\mathbf{u}'T'}^{\mathrm{rot}} = \gamma \hat{\mathbf{k}} \times \nabla \overline{T'^2} \tag{14}$$

and

$$\gamma \equiv \frac{1}{2}\frac{d\overline{\psi}}{d\overline{T}}.$$

An empirically derived constant for a current system with an equivalent-barotropic vertical structure is $\gamma$, where there is a linear relationship between $\overline{\psi}$ and $\overline{T}$. Rotational EHFs from this result follow temperature variance contours and do not play a dynamical role in net heat advection across a front. The residual component contains all of the divergence

$$\overline{\mathbf{u}'T'}^{\mathrm{div}} = \overline{\mathbf{u}'T'} - \gamma \hat{\mathbf{k}} \times \nabla \overline{T'^2}. \tag{15}$$

The cross-isotherm residual fluxes in Eq. (11) therefore balance the vertical heat flux, which when positive is a measure of the energy conversion from EPE to EKE

$$-\overline{\mathbf{u}'T'}^{\mathrm{div}} \cdot \nabla \overline{T} = \overline{w'T'}\Theta_z. \tag{16}$$

### *b.* MS *method applied to mapped eddy heat fluxes*

The MS method for identifying the divergent component of EHF is revisited for the CPIES-mapped estimates of EHF [Eq. (7)]. For the MS method to hold, mean flow to first order must be along mean temperature contours. In the Kuroshio Extension, the mean upper internal mode currents are an order of magnitude larger than the mean abyssal currents $\overline{\mathbf{u}}_I \gg \overline{\mathbf{u}}_E$. The CPIES-mapped baroclinic velocities flow along mean temperature contours such that mean temperature advection is identically zero, $\overline{\mathbf{u}}_I \cdot \nabla \overline{T} = 0$ and $\overline{\psi}_I = \overline{\psi}_I(\overline{T})$.

With the result that mean baroclinic currents flow along mean temperature contours, the mean baroclinic currents take a functional relationship to the mean temperature in the form

$$f\overline{\mathbf{u}}_I = 2\gamma \mathbf{k} \times \nabla \overline{T}, \tag{17}$$

where $\gamma$ here is

$$\gamma = \frac{1}{2}\frac{d\overline{\psi}_I}{d\overline{T}}.$$

An empirical constant for an equivalent-barotropic system is $\gamma$(MS), where there is an approximately linear relationship between $\overline{\psi}_I$ and $\overline{T}$ (Fig. 5). Here, $\gamma$ is especially linear for temperatures $<14^{\circ}$C at 400-m depth (Fig. 5b). At temperatures $>14^{\circ}$C, the mean streamfunction and temperature field enter the mode water region to the south of the jet (Fig. 3c). Here, the mean temperature contours deviate from parallel isotherms. This does not pose a problem because mean temperature gradients are weak away from the jet and little energy conversion will take place between the mean flow and the eddies.

Using Eq. (17) and substituting it into the mean advection of EPE $\overline{\mathbf{u}}_I \cdot \nabla(1/2)\overline{T'^2}$, it can be shown that the

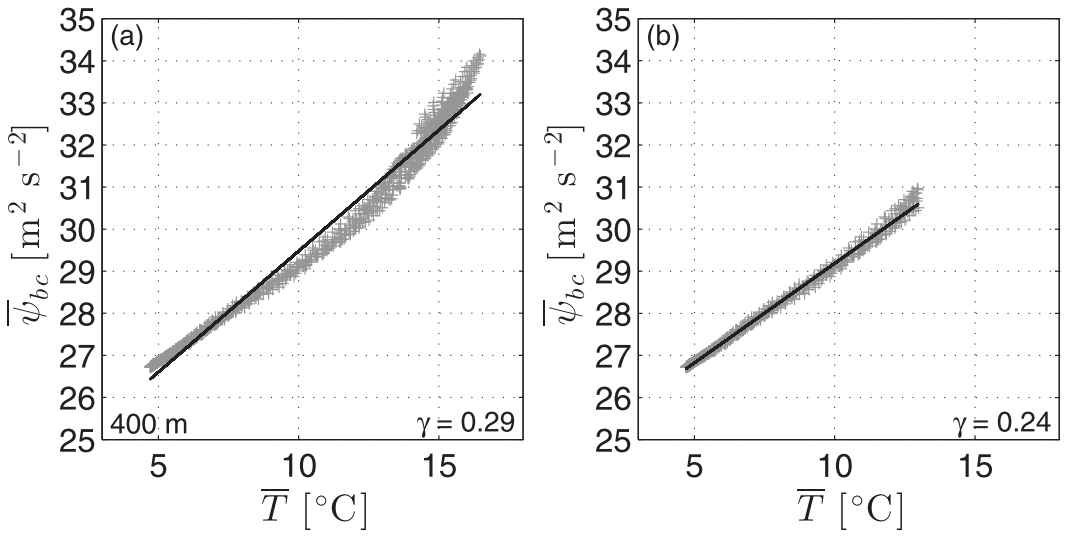


FIG. 5. (a) Scatterplot of mean baroclinic streamfunction vs mean temperature at 400-m depth from the CPIES maps with a linear regression fit to the data. (b) As in (a), but for mean temperature <14°C.

cross-isotherm rotational EHFs balance the mean baroclinic advection of EPE as in Eq. (13)

$$\overline{\mathbf{u}}_I \cdot \nabla \frac{1}{2}\overline{T'^2} + \overline{\mathbf{u}'T'}^{\text{rot}} \cdot \nabla \overline{T} = 0, \tag{18}$$

where the rotational EHFs are the same as in Eq. (14). Because the instantaneous advection of the temperature field by the internal mode currents is zero, the correspondence between $\psi_I'$ and $T'$ and $\overline{\psi}_I$ and $\overline{T}$ is the same and the same empirical constant $\gamma$ is used to define the eddy baroclinic velocity field (Cronin and Watts 1996)

$$f\mathbf{u}_I' = 2\gamma \mathbf{k} \times \nabla T'. \tag{19}$$

Using this result, the internal mode component of the EHF is purely rotational

$$\overline{\mathbf{u}'T'}^{\text{rot}} = \overline{\mathbf{u}_I'T'} = \frac{\gamma}{f}\mathbf{k} \times \nabla \overline{T'^2}. \tag{20}$$

The internal mode EHF is further simplified by setting $f$ to $f_0$ where $f$ is expanded in a Taylor-series expansion about 35°N, $f = f_0 + \beta y$, known as the beta-plane approximation, where $\beta = df/dy$. The internal mode EHF is

$$\overline{\mathbf{u}_I'T'} = \frac{\gamma}{f_0}\mathbf{k} \times \nabla \overline{T'^2} + O(\text{Ro}^2) \tag{21}$$

because in QG flow under relatively small meridional excursions on the globe $\beta y/f_0 = O(\text{Ro}) \ll 1$ so that $\beta$ has only a small effect upon the EHF. The divergence of the EHF to first order is the residual because of the divergence of the EHF associated with the deep reference currents $\mathbf{u}_E$ that are nearly depth independent

$$\nabla \cdot \overline{\mathbf{u}'T'} = \nabla \cdot \overline{\mathbf{u}_E'T'} + O(\text{Ro}^2). \tag{22}$$

The divergence of the internal mode EHF from Eq. (21) vanishes by

$$\nabla \cdot \overline{\mathbf{u}_E'T'} = \frac{\gamma}{f_0}\nabla \cdot \mathbf{k} \times \nabla \overline{T'^2} = \frac{\gamma}{f_0}\left(\frac{\partial^2 \overline{T'^2}}{\partial x \partial y} - \frac{\partial^2 \overline{T'^2}}{\partial x \partial y}\right) = 0. \tag{23}$$

The internal mode component of the EHF is completely rotational and does not play a dynamical role in eddy–mean flow interactions. The external mode component contains all of the divergence. The next section will illustrate from the data the difference in the external and internal eddy heat fluxes.

## EXTERNAL VERSUS INTERNAL FLUXES

Figure 6 shows the decomposition of the EHF for the CPIES maps in the upper ocean at 400 m and the subthermocline ocean at 1500 m superimposed on temperature variance contours. In the upper ocean at 400 m, the total EHF vectors (Fig. 6a) are dominated by the internal EHF vectors (Fig. 6b), and these vectors follow temperature variance contours. In terms of MS, the internal component of the EHF is rotational with EHF

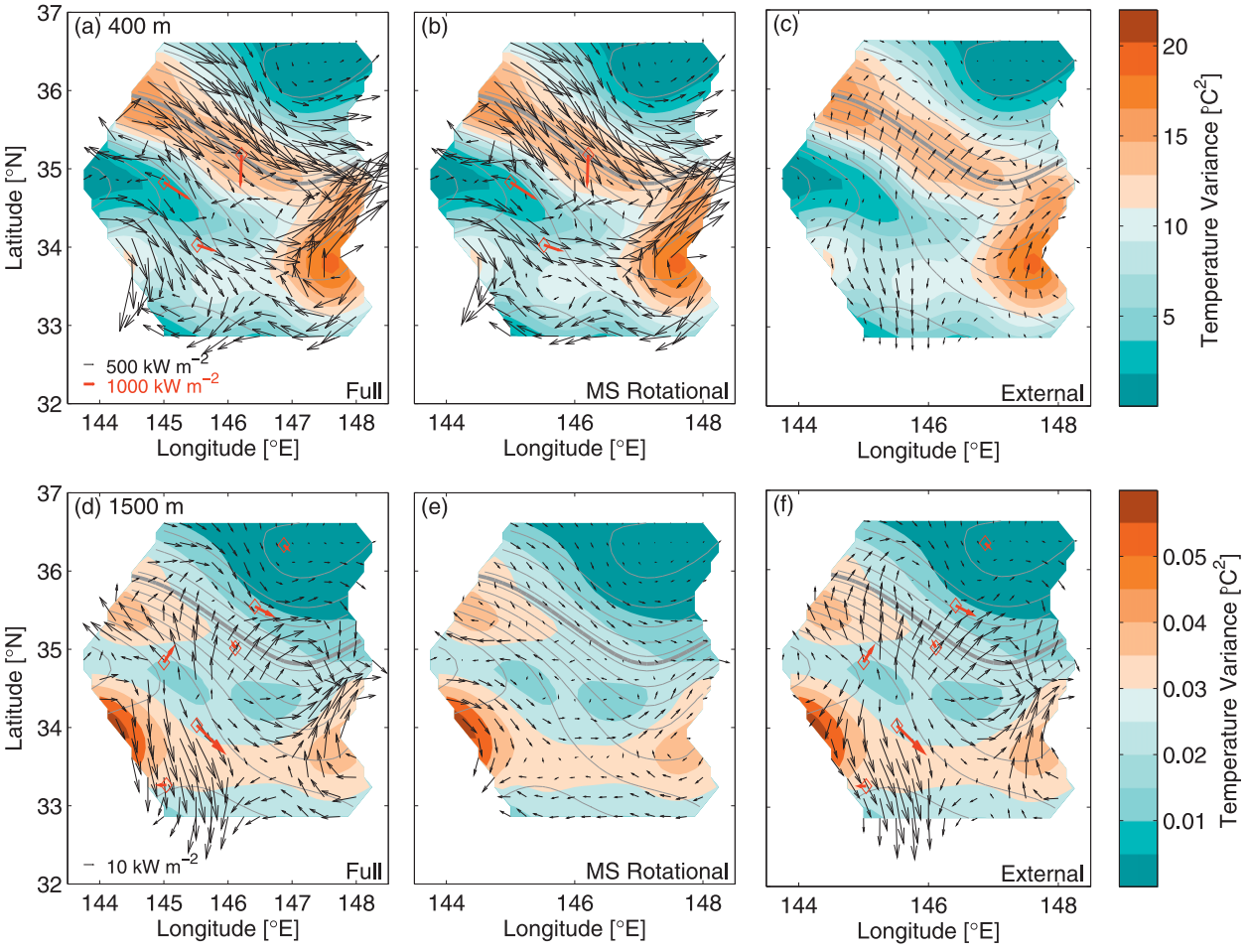


FIG. 6. External vs internal mode EHFs for the upper and deep ocean. EHF vectors superimposed on temperature variance contours (color) and 16-month mean geopotential referenced to 5300-m contours (gray) with a boldface gray contour marking the mean axis of the current. (a) 400-m total EHF vectors, (b) internal (MS rotational) EHF vectors, and (c) external EHF vectors. (d)–(f) As in (a)–(c), but for 1500 m. Red diamonds and red arrows illustrate the good agreement at the mooring locations and heat flux vectors at 250 m in (a) and (b) and at 1500 m in (d) and (f).

vectors rotating anticyclonically around temperature variance hot spots in the northwest, southwest, and southeast parts of the KESS array. The external component of the EHF (Fig. 6c), which contains the divergence, is much weaker in magnitude than the internal component and does not necessarily follow temperature variance contours. Separated in this way, the masking by the internal component is removed.

In the subthermocline ocean at 1500 m, the internal and external components of the EHF are comparable in magnitude (Figs. 6d–f). The internal component again is completely rotational with vectors that follow the temperature variance contours (Fig. 6e). The external component is much stronger in magnitude near the mean path of the jet and is responsible for cross-frontal heat exchange with vectors that don't necessarily follow temperature variance contours.

Figure 6 demonstrates that the rotational EHFs are strongest in the upper ocean and decrease in magnitude with depth. The traditional estimates in section 3 reveal that the estimates from the moorings in Fig. 3c are similarly oriented to the external component of the subthermocline (1500 m) fluxes in Fig. 6f. Moreover in the upper ocean this may explain why K4, K5, and K8 had such strong equatorward heat fluxes at 250 m (Table 1) because Fig. 6b reveals that the rotational fluxes near those sites at 400 m have large negative meridional components.

It is noted here that the external EHFs are not rotation free, but a large known rotational component (internal) of the EHF has been removed from the full signal. Cronin (1996) also noted that the residual fluxes, using the MS method in the Gulf Stream, were not rotation free as well. Interpretation of the external fluxes

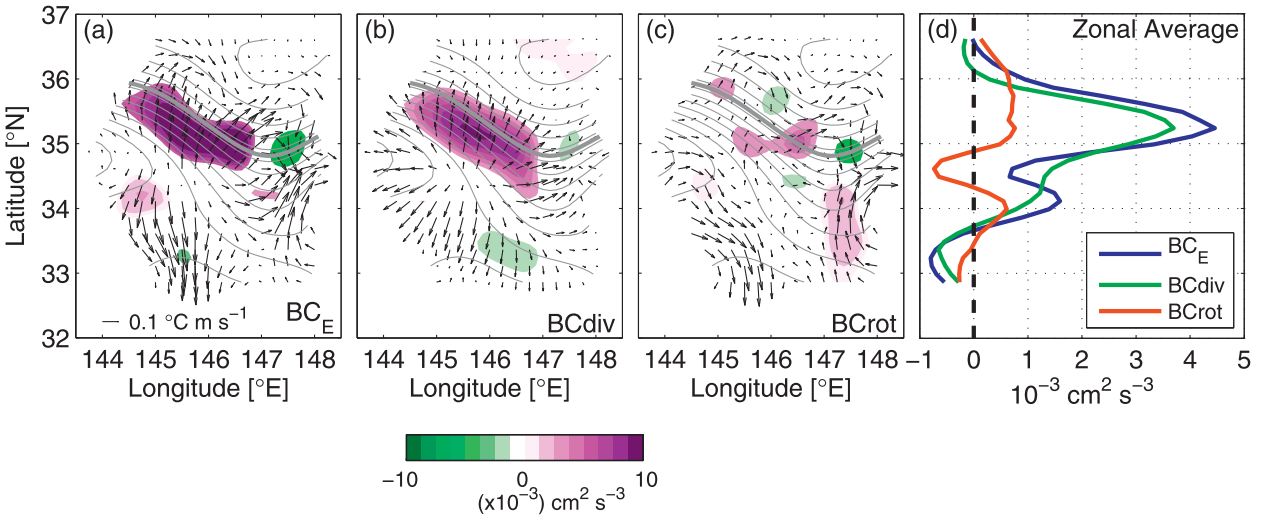


FIG. 7. (a) Decomposition of $\overline{\mathbf{u}'_E T'}$ vectors into (b) divergent and (c) rotational components at 400-m depth. The BC is superimposed with color contours (CI = 0.5 $\mathrm{cm^2\,s^{-3}}$). Contour lines show the mean geopotential referenced to 5300 m (gray contours, CI = 1 $\mathrm{m^2\,s^{-2}}$). The boldface gray contour marks the mean axis of the jet (38.52 $\mathrm{m^2\,s^{-2}}$ geopotential contour, equivalent to where the 12°C isotherm crosses the 300 m isobath). (d) Zonally averaged BC in (a)–(c).

should be more representative of the divergent fluxes as will be demonstrated in the next section.

## 6. Divergent eddy heat flux and relation to energy conversion

While the external EHFs contain all of the divergent component, they may also contain a rotational component. Consequently, the $\overline{\mathbf{u}'_E T'}$ fields were further decomposed into "purely" divergent and rotational components in accord with Helmholtz's theorem

$$\overline{\mathbf{u}'_E T'} = \overline{\mathbf{u}'_E T'}^{\,\mathrm{div}} + \overline{\mathbf{u}'_E T'}^{\,\mathrm{rot}} \tag{24}$$

using objective analysis (OA), with nondivergent correlation functions, as discussed in the appendix. The OA method maps the best-fit nondivergent vector field to the total EHF field. The divergent component of the external EHF is determined by taking the difference between the full vector field and the best-fit nondivergent field from the OA

$$\overline{\mathbf{u}'T'}^{\,\mathrm{div}} = \overline{\mathbf{u}'_E T'} - \overline{\mathbf{u}'_E T'}^{\,\mathrm{OA}}. \tag{25}$$

The subscript $E$ has been dropped from the eddy velocity term for the divergent flux for convenience.

The decomposition of the external EHF field into divergent and rotational components at 400-m depth, which is approximately the midthermocline depth, is shown in Fig. 7. Traditionally (Bryden 1979; Cronin and Watts 1996; Phillips and Rintoul 2000), if sufficient data are available, the product of EHF with the mean horizontal temperature gradient is estimated, which is a measure of the energy conversion from mean potential energy (MPE) to EPE

$$\mathrm{BC} = -\frac{\alpha g}{\Theta_z}\overline{\mathbf{u}'T'} \cdot \nabla\overline{T}. \tag{26}$$

The baroclinic conversion (BC) is superimposed on the EHF vectors to compare between the rotational and divergent and combined fields (Fig. 7). BC quantified from the external mode velocities, using $\overline{\mathbf{u}'_E T'}$ in Eq. (26) to give $\mathrm{BC}_E$ in Fig. 7a, is mostly positive, peaking at $14 \times 10^{-3}\,\mathrm{cm^2\,s^{-3}}$ along the mean path upstream of the mean trough. The BC estimate, improved by removing its nondivergent rotational component [Eq. (25)], produces the best estimate of cross-isotherm DEHFs (BCdiv), shown in Fig. 7b. BCdiv has a nearly identical spatial structure to $\mathrm{BC}_E$, but with a reduced magnitude that is 60%–80% of $\mathrm{BC}_E$ and peaks at $10 \times 10^{-3}\,\mathrm{cm^2\,s^{-3}}$ along the mean path upstream of the mean trough. The contribution to BC by the cross-isotherm components of rotational EHF is denoted BCrot, which is found to be small (Fig. 7c). The level of agreement between $\mathrm{BC}_E$ and BCdiv is reiterated in Fig. 7d, which shows the latitudinal dependence of the zonally averaged BCs from Figs. 7a–c. The point of this figure is to illustrate that the external EHF conversion values ($\propto -\overline{\mathbf{u}'_E T'} \cdot \nabla\overline{T}$) are a good approximation to the DEHF conversion ($\propto -\overline{\mathbf{u}'T'}^{\,\mathrm{div}} \cdot \nabla\overline{T}$). Hence, in this region where the currents are represented by the sum of an equivalent-barotropic internal mode plus a nearly depth-independent

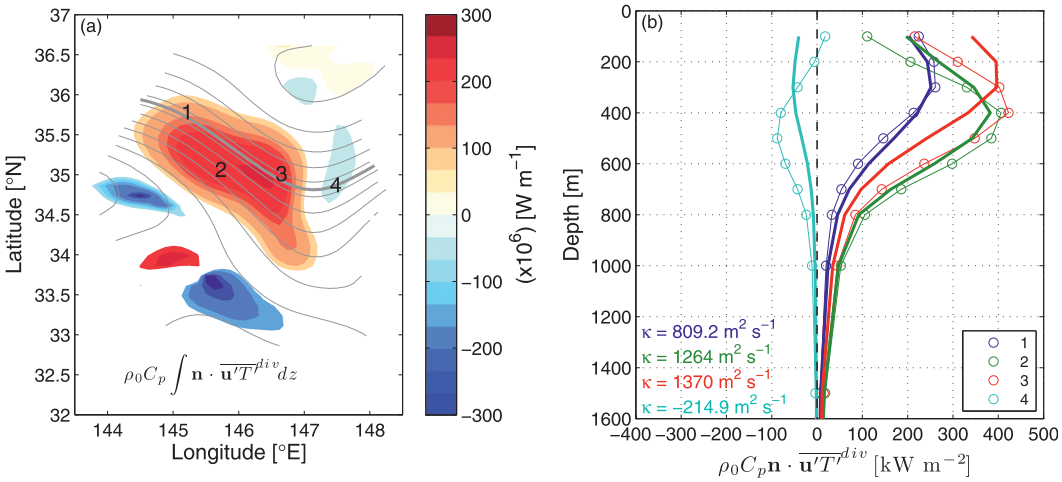


FIG. 8. Vertical structure of the divergent EHFs along the mean path. (a) Vertically integrated meridional component of the divergent EHF superimposed on the 16-month mean geopotential referenced to 5300 m (gray contours). The boldface gray contour marks the axis of the jet (38.52 $m^2 s^{-2}$ geopotential contour, equivalent to where the 12°C isotherm crosses the 300 m isobath). (b) Vertical profiles of the cross-stream divergent EHF at the numbered positions indicated in (a). Circles are observations and boldface lines are $\mathbf{n} \cdot \overline{\mathbf{u}'T'}^{\text{div}} = -\kappa \partial \overline{T}/\partial n$ for best-fit $\kappa$.

external mode, the upper-ocean purely divergent heat fluxes can be well represented by the simple product of the external current $\mathbf{u}'_E$ and upper-temperature $T'$.

### a. Horizontal structure

The horizontal structure of the 16-month DEHFs are shown in Fig. 7b for the midthermocline depth of 400 m. Along the Kuroshio mean path, the DEHFs are mostly downgradient and strongest upstream of the mean trough at ~147°E. A similar spatial structure in DEHF was also observed in the Gulf Stream at 68°W about a mean trough from an array of current meters and inverted echo sounders from the Synoptic Ocean Prediction Experiment (SYNOP) (Cronin and Watts 1996).

Away from the mean path, DEHFs were weak to the north. South of the jet near 33°N and 145.5°E, there is a region of strong equatorward heat flux; however, BCdiv is weak there because the mean temperature gradient is small away from the jet.

### b. Vertical structure

The vertical structure of the cross-stream DEHF $\rho_0 C_p \mathbf{n} \cdot \overline{\mathbf{u}'T'}^{\text{div}}$, where

$$\mathbf{n} = -\frac{\nabla \overline{T}}{|\nabla \overline{T}|} \tag{27}$$

is the cross-stream unit vector 90° to the left of the along-stream motion, is presented in this section. The vertical structure is plotted in Fig. 8b at four locations of extrema along the mean path: three upstream of the mean trough where fluxes were downgradient and one downstream where the fluxes were weakly upgradient (Fig. 8a). From the profiles, it is evident that the magnitudes of the fluxes reach a subsurface maximum near 400 m at ~400 kW $m^{-2}$ in some places. We next discuss two questions. How well can the DEHF be parameterized by eddy diffusivity, and why does its subsurface maximum occur where it does?

#### 1) HEAT FLUX PARAMETERIZATION

Eddy fluxes are often parameterized as Fickian, where the eddy flux is taken to be diffusive and the temperature is diffused down the mean temperature gradient (e.g., Gent and McWilliams 1990). Figure 7b suggests that this type of parameterization may hold for the KESS observations. If the DEHFs are parameterized in this way they take the form

$$\overline{\mathbf{u}'T'}^{\text{div}} = -\kappa \nabla \overline{T}, \tag{28}$$

where $\kappa$ is an eddy diffusivity. Using this parameterization, a constant eddy diffusivity with depth $\kappa$ was fitted for the four sites in Fig. 8b from a least squares fit to the equation

$$\mathbf{n} \cdot \overline{\mathbf{u}'T'}^{\text{div}} + \kappa \frac{\partial \overline{T}}{\partial n} = \epsilon, \tag{29}$$

where $\partial/\partial n = \mathbf{n} \cdot \nabla$, and $\epsilon$ is the difference between the observed and fitted cross-isotherm EHF, for which the sum of the squares is minimized. This parameterization tends to hold true in the upstream part of the flow where sites 1, 2, and 3 match very well with constant eddy

diffusivities of 809, 1264, and 1370 $m^2 s^{-1}$, respectively. A weakly negative $\kappa$ would be required downstream of the mean trough at site 4 to correspond to EHF that has an upgradient component and is consequently not dissipative at that location. Smith and Marshall (2009) found that a constant eddy diffusivity of 1000 $m^2 s^{-1}$ for buoyancy fluxes matched observations well in the Southern Ocean to the south of Tasmania, but their study did not make any distinctions between divergent and rotational fluxes. Eddy diffusivities in the Kuroshio Extension estimated from Eq. (29), but for the total EHF $\overline{\mathbf{u}'_E T'}$, are several times larger (up to 3000 $m^2 s^{-1}$) than $\kappa$ estimated from the divergent component. The rotational EHFs make $\kappa$ seem artificially high.

### 2) Heat flux maximum at inflection point of PV

The depth where the DEHFs reach a maximum upstream of the mean trough is also where the mean QG potential vorticity (PV) gradient changes sign in the vertical. It is a necessary condition for baroclinic instability that the QGPV gradient changes sign in the vertical (Charney and Stern 1962; Pedlosky 1964) (referred to as CSP conditions). Note that necessary conditions for baroclinic instability can also be met at the boundaries based on CSP. The mean QGPV for a Boussinesq fluid is

$$\overline{q} = \beta y + \overline{\zeta} + f_0 \frac{\partial}{\partial z}\left(\frac{\overline{\tilde{T}}}{\Theta_z}\right), \tag{30}$$

where $\zeta$ is the relative vorticity, $\tilde{T} = T - \Theta(z)$, and the last term on the rhs is referred to as the stretching vorticity. In strong vertically sheared flow, $\beta y$ is an order of magnitude smaller than the other terms in Eq. (30) and to first order the mean relative vorticity is small $O(0.1f)$, such that the mean QGPV is approximately equal to stretching vorticity.

The mean cross-stream QGPV gradient in stream coordinates (**s**, **n**, and **k**), where $\mathbf{s} = \mathbf{n} \times \mathbf{k}$ is the along-stream unit vector and **n** [Eq. (27)] is 90° to the left, is

$$\frac{\partial \overline{q}}{\partial n} = \frac{\partial}{\partial z}\left(\frac{f_0}{\Theta_z}\frac{\partial \overline{\tilde{T}}}{\partial n}\right) = -\frac{\partial}{\partial z}\left(\frac{f_0^2}{N^2}\frac{\partial \overline{u}_s}{\partial z}\right), \tag{31}$$

where $\overline{u}_s = \mathbf{s} \cdot \overline{\mathbf{u}}_I$ is the along-stream mean baroclinic flow in thermal wind balance

$$\frac{\partial \overline{u}_s}{\partial z} = -\frac{\alpha g}{f_0}\frac{\partial \overline{\tilde{T}}}{\partial n}, \tag{32}$$

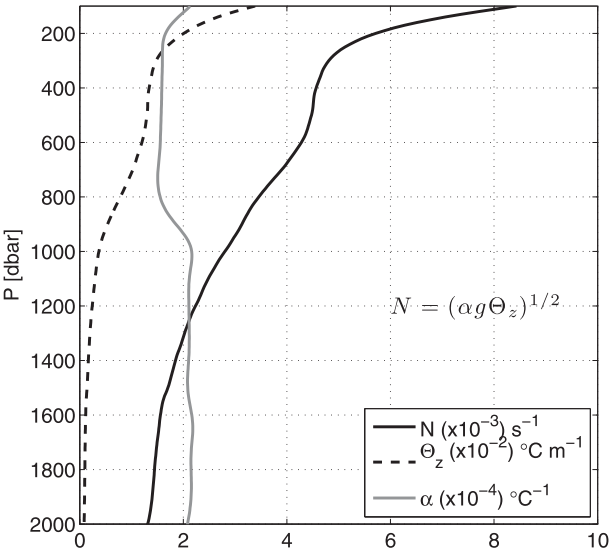


FIG. 9. The regional-average background buoyancy frequency ($N$), potential temperature gradient (i.e., $\Theta_z$), and effective thermal expansion coefficient (i.e., $\alpha$) profiles. All values were scaled as in key.

$N^2(z) = \alpha g \Theta_z$ is the buoyancy frequency of the regional background field, and a simple equation of state was assumed $\tilde{\rho} = \rho_0(1 - \alpha \tilde{T})$.

At the depth of the maximum flux $z_c$ its vertical derivative is zero, so differentiating Eq. (28) and Eq. (32) in the vertical gives

$$\frac{\partial}{\partial z}(\mathbf{n} \cdot \overline{\mathbf{u}' T'^{\mathrm{div}}})\bigg|_{z_c} = -\kappa \frac{\partial}{\partial z}\frac{\partial \overline{\tilde{T}}}{\partial n}\bigg|_{z_c} = \kappa \frac{\partial}{\partial z}\left(\frac{f_0}{\alpha g}\frac{\partial \overline{u}_s}{\partial z}\right)\bigg|_{z_c} = 0. \tag{33}$$

The regional-mean profiles of buoyancy frequency and $\alpha$ (Fig. 9) are nearly constant in the vicinity of maximum fluxes and can be pulled out of the vertical derivative. From this result the depth at which the fluxes reach a maximum is also the depth at which the mean QGPV changes sign and is an inflection point in the mean along-streamflow

$$\frac{\partial \overline{q}}{\partial n} \propto \frac{\partial^2 \overline{u}_s}{\partial z^2} = 0, \quad \text{at} \quad z = z_c, \tag{34}$$

where $z_c$ is the depth of the maximum fluxes. Figure 10 shows the vertical cross section of DEHFs at two locations along the mean path upstream of the mean diffluent trough. The inflection point of the vertical shear approximately follows the maximum envelope of the flux shoaling to the north approximately following the $26.5\sigma_\theta$ surface. This is also in agreement with the result from

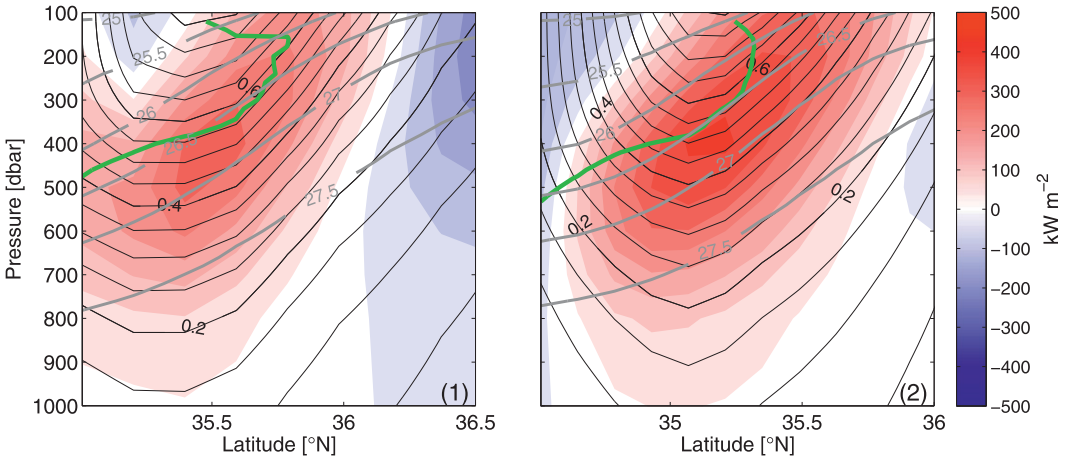


FIG. 10. (left) Cross-stream profile of the mean cross-stream divergent EHF (color contours) at location 1 in Fig. 8 superimposed on the mean along streamflow (black contours; m s$^{-1}$), mean potential density contours (gray contours), and the depth of the inflection point in the along streamflow (green contour). (right) As in the left panel, but for location 2 in Fig. 8. The maximum divergent EHFs occur near this inflection point.

Tulloch et al. (2011) that westerly sheared flows such as the ACC, Kuroshio Extension, and Gulf Stream are characterized by Phillips-like baroclinic instability with a QGPV gradient sign change in the interior.

## 7. Meridional eddy heat transport

In this section, the eddy heat transport is estimated from the CPIES maps and put into the context of previous studies. The meridional eddy heat transport $Q_{ve}$ is defined as the vertically integrated meridional EHF between 100- and 5300-m depth

$$Q_{ve} = \rho_0 C_p \int_{-H_{\mathrm{ref}}}^{-H_{\mathrm{Ek}}} \overline{v'T'}\, dz. \qquad (35)$$

Here, $Q_{ve}^{\mathrm{tot}}$ estimated from the full EHF field [Eq. (7)] and $Q_{ve}^{\mathrm{div}}$ estimated from the DEHF field [Eq. (25)] are shown in Figs. 11a,b, respectively; $Q_{ve}^{\mathrm{tot}}$ is five times larger than $Q_{ve}^{\mathrm{div}}$, and the spatial structure of the meridional component of $Q_{ve}$ in Fig. 11a has a very different structure than the divergent field in Fig. 11b. The total transport vectors tend to follow the mean streamlines of the flow in Fig. 11a giving rise to negative $Q_{ve}^{\mathrm{tot}}$ upstream and positive downstream of the mean trough. Contrary to the total transport, $Q_{ve}^{\mathrm{div}}$ is positive along the mean path with negative transport to the south of the jet between 33° and 34°N.

For comparison, Qiu and Chen (2005a) estimated the total eddy heat transport over a 6-yr time frame from a combination of Argo floats, sea surface temperature (SST) from Tropical Rainfall Measuring Mission

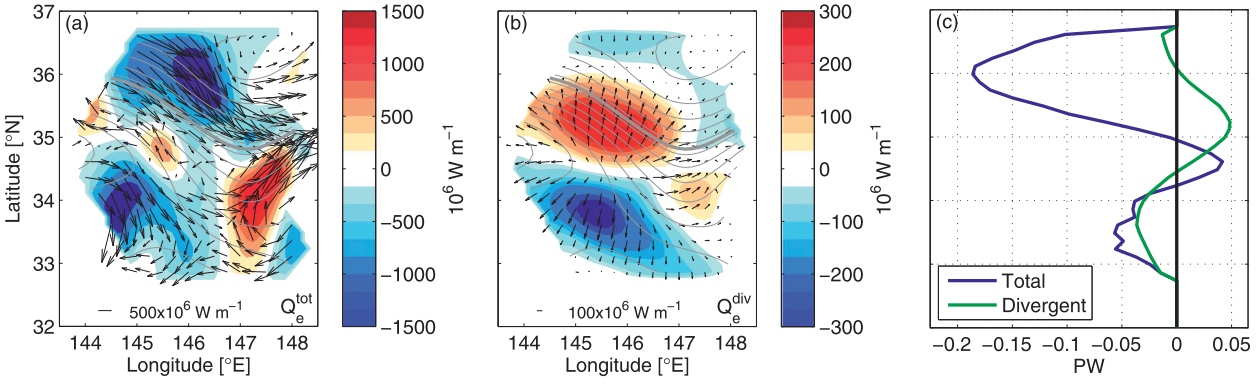


FIG. 11. (a) Total eddy heat transport vectors with the meridional component contoured in color (CI = 250 W m$^{-1}$) superimposed on the 16-month mean geopotential referenced to 5300 m (gray contours, CI = 1 m$^2$ s$^{-2}$) with the boldface gray contour marking the axis of the jet (38.52 m$^2$ s$^{-2}$ geopotential contour, equivalent to where the 12°C isotherm crosses the 300 m isobath). (b) As in (a), but for divergent eddy heat transport. (c) Zonally integrated meridional eddy heat transport.

(TRMM) Microwave Imager data, and SSH data from satellite altimetry in the Kuroshio Extension region. It is noted that their study did not make any distinctions between divergent and rotational eddy heat transport. When comparing $Q_{ve}^{\text{tot}}$ in Fig. 11a with their Fig. 13 in Qiu and Chen (2005a) there are remarkable similarities in the spatial structure within the KESS array given the different averaging times but the magnitudes differ. The differences in magnitude may arise because Qiu and Chen (2005a) multiplied the surface heat flux by an effective depth $H_e$ of 177 m estimated from Argo float observations, whereas this study is an estimate throughout the entire water column. It has also been argued that Argo float observations underestimate EHF because they do not provide a high enough sampling frequency (Chinn and Gille 2007).

Zonally integrating the meridional eddy heat transport from the western to eastern boundary of the KESS array between 144° and 148°E displays the latitudinal dependence (Fig. 11c). As noted above, the pattern of negative (i.e., equatorward) total heat flux corresponds to this path segment of the Kuroshio Extension that enters a mean trough. In contrast, the divergent meridional heat transport is positive (i.e., poleward) along the mean path of the jet axis and sums to 0.05 PW at 35.25°N. For context, Trenberth and Caron (2001) estimate in their Fig. 6 the global oceanic heat transport near 35°N to be less than 0.5 PW, of which the Pacific accounts for a relatively small portion. Volkov et al. (2008), which was an update of Jayne and Marotzke (2002), estimate 0.15 PW across the entire Pacific at 36°N from the Estimating the Circulation and Climate of the Ocean, Phase II (ECCO2) model simulations. Therefore the divergent eddy heat transport in KESS may account for ~1/3 of the total Pacific poleward heat transport. The Pacific Ocean is ~10000-km wide at 35°N, which means that the KESS region accounts for ~1/10 the size of the Pacific and accounts for a substantial amount of the meridional heat transport at this latitude.

## 8. Discussion and conclusions

The KESS experiment provided unprecedented observations to quantify EHF with the mesoscale resolved. Traditional estimates of EHF from sparse current meter moorings had been difficult to interpret because of large rotational fluxes that mask the important divergent fluxes. Using an array of CPIES that provided three-dimensional maps of the absolute geostrophic current and temperature field for 16 months, mean EHFs were quantified. Geostrophic currents from the CPIES array determine the vertical structure as the vector sum of an equivalent-barotropic internal mode $\mathbf{u}_I$ and a nearly depth-independent external mode $\mathbf{u}_E$, and this separation makes it possible to distinguish between divergent and rotational EHF. The dynamically important DEHFs were revealed to be driven by the correlation between the external mode geostrophic currents and the upper thermal front $\overline{\mathbf{u}_E' T'}$. In the context of MS, the EHF associated with the equivalent-barotropic internal mode geostrophic currents $\overline{\mathbf{u}_E' T'}$ were completely rotational and played no dynamical role.

Here, $\overline{\mathbf{u}_E' T'}$ was further decomposed into "purely" divergent and rotational components using OA. The structure of the cross-isotherm DEHF nearly conformed to the full fluxes $\overline{\mathbf{u}_E' T'}$, but its magnitude was 60%–80% as large. The 16-month mean DEHF maps revealed a spatial structure that was mostly downgradient and strongest upstream of a mean trough at ~147°E. An eddy energetics analysis showed that the downgradient DEHFs (BCdiv) had a mean-to-eddy potential energy conversion maximum of $10 \times 10^{-3}\,\text{cm}^2\,\text{s}^{-3}$ with a depth-averaged value of $3 \times 10^{-3}\,\text{cm}^2\,\text{s}^{-3}$. A positive mean-to-eddy energy conversion rate in KESS suggests there is not a stabilization point within the first meander region at 144°–148°E. Waterman et al. (2011) claim that a stabilization point in the along streamflow resides downstream of the KESS observations and our results do not confirm nor contradict this. The Kuroshio Extension between 144° and 148°E is still in a region of eddy growth.

The vertical structure of the DEHFs fit well to a downgradient parameterization proportional to the mean temperature gradient via constant eddy diffusivity $\kappa$, which ranged rather narrowly from 800 to $1400\,\text{m}^2\,\text{s}^{-1}$ along the mean path. DEHFs had a subsurface maximum in excess of $400\,\text{kW}\,\text{m}^{-2}$ near 400-m depth.

Two concepts suggest intriguingly different depths where eddy mixing should be greatest, the familiar steering-level argument, versus the location where the necessary condition for baroclinic instability is met. Many studies have attributed middepth enhancement of eddy mixing to steering levels, such as recent Southern Ocean studies by (Smith and Marshall 2009; Abernathey et al. 2010; Klocker et al. 2012). Steering levels are regions where the phase speed $c$ of a growing eastward-propagating meander matches the mean flow $|\overline{u}_s - c| \to 0$. The maximum DEHFs occurred where the mean along streamflow is $\sim 50\,\text{cm}\,\text{s}^{-1}$. This is not a steering level in the Kuroshio Extension because phase speeds for propagating meanders are substantially less than $50\,\text{cm}\,\text{s}^{-1}$ for periods of 5–40 days (Tracey et al. 2012). Ferrari and Nikurashin (2010) discuss that there may be an overemphasis on the importance of steering levels in eddy mixing, because the theory takes a linear view of eddies as periodic waves. Alternatively, eddy mixing should properly be based upon eddy diffusivity $K$ of PV, and

one may postulate that eddy processes cause related diffusivities for heat and PV, $\kappa$, and $K$. Because $K$ is proportional to the inverse of the QGPV lateral gradient, it might be expected that $K$ would reach a maximum where the QGPV lateral gradient passes through zero. The sign change in QGPV lateral gradient signifies the necessary condition for baroclinic instability, and as shown in section 6 from thickness PV its approximate indicator is an inflection point in the along-stream current speed $\partial^2\overline{u}_s/\partial z^2 = 0$. Maximum subsurface cross-stream DEHFs were confirmed in (Fig. 10) to occur near this depth.

The final section demonstrated the large differences between estimating eddy heat transport based on the total transport and based on the divergent transport. The total eddy heat transport tended to follow the mean path of the jet. A large negative meridional eddy heat transport occurred where the jet enters a mean trough. The mostly downgradient divergent fluxes summed to a positive divergent meridional eddy heat transport of 0.05 PW at 35.25°N, which accounts for about 1/3 of the northward ocean heat transport spanning the Pacific at this latitude.

*Acknowledgments.* We thank two anonymous reviewers for their comments which improved this manuscript. We thank the captains and crews of the R/V *Thompson*, R/V *Revelle*, and R/V *Melville*. The CPIES were successfully developed, deployed, and recovered by G. Chaplin and E. Sousa with the assistance of Gary Savoy and Cathy Cipolla at the URI Equipment Development Laboratory. We also thank Karen Tracey and Andy Greene for help in processing and mapping the CPIES data. We appreciate additional current meter mooring data supplied by our colleagues at Woods Hole Oceanographic Institution, S. Jayne and N. Hogg, and at the Applied Physics Laboratory of the University of Washington, L. Rainville. This work was supported by the US National Science Foundation under Grants OCE02-21008 and OCE08-51246.

## APPENDIX

### Objective Analysis

A method that can be used to further decompose the eddy fluxes into ''purely'' rotational and divergent components utilizes OA, with nondivergent correlation functions. The advantage of this procedure is that, as Bretherton et al. (1976) showed, when the correlation functions for vector variables in the OA correlation matrices are nondivergent, the output vectors are the best-fitted estimates of the nondivergent field.

The OA method adopted from Bretherton et al. (1976) in Watts et al. (2001a) and summarized here has the generalized goal of mapping vector variables ($\mu$, $\nu$) from limited observations with noise and constrained to be nondivergent. In this particular case the $\mu = \overline{u'T'}$ and $\nu = \overline{v'T'}$ are zonal and meridional components of eddy heat flux (rather than the usual geostrophic current components). For their nondivergent rotational component, there exists a streamfunction $\psi(x, y, t)$ such that

$$\mu^{\text{rot}} = -\frac{\partial\psi}{\partial y} \quad \text{and} \quad \nu^{\text{rot}} = \frac{\partial\psi}{\partial x}.$$

This linear least squares minimization method utilizes cross-covariance functions whose $x$ and $y$ derivatives are nondivergent. For this study, the correlation function for $\psi$ is taken to be

$$F_{\psi\psi} = F = e^{-\lambda r^2} \quad \text{and} \quad F' = \frac{dF}{dr} = -2\lambda r F,$$

which is isotropic in separation distance $\gamma = (\delta x^2 + \delta y^2)^{1/2}$. We used correlation length $L = \lambda^{-1/2} = 75$ km, based on the observed correlation length found in KESS by Donohue et al. (2010) for geostrophic pressures. (We reasoned simply that the ocean currents drove the eddy fluxes, and we used the correlation scale for the deep eddies.)

The cross-correlation functions for the $\mu$ and $\nu$ components are

$$F_{\mu\mu} = 2\lambda[1 - 2\lambda(\delta y)^2]F,$$

$$F_{\nu\nu} = 2\lambda[1 - 2\lambda(\delta x)^2]F, \quad \text{and}$$

$$F_{\mu\nu} = F_{\nu\mu} = 4\lambda^2(\delta x)(\delta y)F.$$

## REFERENCES

Abernathey, R., J. Marshall, M. Mazloff, and E. Shuckburgh, 2010: Enhancement of mesoscale eddy stirring at steering levels in the Southern Ocean. *J. Phys. Oceanogr.,* **40,** 170–184.

Bishop, S. P., 2012: The role of eddy fluxes in the Kuroshio Extension at 144°–148°E. Ph.D. thesis, University of Rhode Island, 128 pp.

——, D. R. Watts, J.-H. Park, and N. G. Hogg, 2012: Evidence of bottom-trapped currents in the Kuroshio Extension region. *J. Phys. Oceanogr.,* **42,** 321–328.

Bower, A. S., and N. G. Hogg, 1996: Structure of the Gulf Stream and its recirculations at 55°W. *J. Phys. Oceanogr.,* **26,** 1002–1022.

Bretherton, F. P., E. Davis, and C. B. Fandry, 1976: A technique for objective analysis and design of oceanographic experiments applied to MODE-73. *Deep-Sea Res.,* **23,** 559–582.

Bryden, H. L., 1979: Poleward heat flux and conversion of available potential energy in Drake Passage. *J. Mar. Res.,* **37,** 1–22.

Charney, J. G., and M. E. Stern, 1962: On the stability of internal baroclinic jets in a rotating atmosphere. *J. Atmos. Sci.,* **19,** 159–172.

Chinn, B. S., and S. T. Gille, 2007: Estimating eddy heat flux from float data in the North Atlantic: The impact of temporal sampling interval. *J. Phys. Oceanogr.,* **24,** 923–934.

Cronin, M., 1996: Eddy–mean flow interaction in the Gulf Stream at 68°W. Part II: Eddy forcing on the time-mean flow. *J. Phys. Oceanogr.,* **26,** 2132–2151.

——, and D. R. Watts, 1996: Eddy–mean flow interaction in the Gulf Stream at 68°W. Part I: Eddy energetics. *J. Phys. Oceanogr.,* **26,** 2107–2131.

Dewar, W. K., and J. M. Bane, 1989: Gulf Stream dynamics. Part I: Mean flow dynamics at 73°w. *J. Phys. Oceanogr.,* **19,** 1558–1573.

Donohue, K. A., D. R. Watts, K. L. Tracey, A. D. Greene, and M. Kennelly, 2010: Mapping circulation in the Kuroshio Extension with an array of current and pressure recording inverted echo sounders. *J. Atmos. Oceanic Technol.,* **27,** 507–527.

Ducet, N., and P. Y. Le-Traon, 2001: A comparison of surface eddy kinetic energy and Reynolds stresses in the Gulf Stream and the Kuroshio Current systems from merged TOPEX/Poseidon and *ERS-1/2* altimetric data. *J. Geophys. Res.,* **106** (C8), 16 603–16 622.

Emery, W. J., and R. E. Thomson, 2001: *Data Analysis Methods in Physical Oceanography*. 2nd ed. Elsevier, 654 pp.

Ferrari, R., and M. Nikurashin, 2010: Suppression of eddy diffusivity across jets in the Southern Ocean. *J. Phys. Oceanogr.,* **40,** 1501–1519.

Fox-Kemper, B., R. Ferrari, and J. Pedlosky, 2003: On the indeterminacy of rotational and divergent eddy fluxes. *J. Phys. Oceanogr.,* **33,** 478–483.

Gent, P. R., and J. C. McWilliams, 1990: Isopycnal mixing in ocean circulating models. *J. Phys. Oceanogr.,* **20,** 150–155.

Greene, A. D., 2010: Deep variability in the Kuroshio Extension. Ph.D. thesis, University of Rhode Island, 150 pp.

Hall, M. M., 1986: Assessing the energetics and dynamics of the Gulf Stream at 68°W from moored current measurements. *J. Mar. Res.,* **44,** 423–433.

——, 1991: Energetics of the Kuroshio Extension at 35°N, 152°E. *J. Phys. Oceanogr.,* **21,** 958–975.

Hogg, N. G., 1986: On the correction of temperature and velocity time series for mooring motion. *J. Atmos. Oceanic Technol.,* **3,** 204–214.

——, and D. E. Frye, 2007: Performance of a new generation of acoustic current meters. *J. Phys. Oceanogr.,* **37,** 148–161.

Howe, P. J., K. A. Donohue, and D. R. Watts, 2009: Stream-coordinate structure and variability of the Kuroshio Extension. *Deep-Sea Res.,* **56,** 1093–1116.

Illari, L., and J. C. Marshall, 1983: On the interpretation of eddy fluxes during a blocking episode. *J. Atmos. Sci.,* **40,** 2232–2242.

Jayne, S. R., and J. Marotzke, 2002: The oceanic eddy heat transport. *J. Phys. Oceanogr.,* **32,** 3328–3345.

——, and Coauthors, 2009: The Kuroshio Extension and its recirculation gyres. *Deep-Sea Res. I,* **56,** 2088–2099.

Killworth, P. D., 1992: An equivalent-barotropic mode in the fine resolution Antarctic model. *J. Phys. Oceanogr.,* **22,** 1379–1387.

Klocker, A., R. Ferrari, and J. H. LaCasce, 2012: Estimating suppression of eddy mixing by mean flows. *J. Phys. Oceanogr.,* **46,** 1566–1576.

Marshall, J., and G. Shutts, 1981: A note on rotational and divergent eddy fluxes. *J. Phys. Oceanogr.,* **11,** 1677–1679.

Meinen, C. S., 2008: Accuracy in mooring motion temperature corrections. *J. Atmos. Oceanic Technol.,* **25,** 2293–2303.

——, and D. R. Watts, 1998: Calibrating inverted Echo sounders equipped with pressure sensors. *J. Atmos. Oceanic Technol.,* **15,** 1339–1345.

Mizuno, K., and W. B. White, 1983: Annual and interannual variability in the Kuroshio Current system. *J. Phys. Oceanogr.,* **13,** 1847–1867.

Park, J.-H., D. R. Watts, K. A. Donohue, and K. L. Tracey, 2012: Comparisons of sea surface height variability observed by pressure-recording inverted echo sounders and satellite altimetry in the Kuroshio Extension. *J. Oceanogr.,* **68,** 401–416.

Pedlosky, J., 1964: The stability of currents in the atmosphere and ocean: Part I. *J. Atmos. Sci.,* **21,** 201–219.

Phillips, H. E., and S. R. Rintoul, 2000: Eddy variabillity and energetics from direct current measurements in the Antarctic Circumpolar Current south of Australia. *J. Phys. Oceanogr.,* **30,** 3050–3076.

Qiu, B., and S. Chen, 2005a: Eddy-induced heat transport in the subtropical North Pacific from Argo, TMI, and altimetry measurements. *J. Phys. Oceanogr.,* **35,** 458–473.

——, and ——, 2005b: Variability of the Kuroshio Extension jet, recirculation gyre, and mesoscale eddies on decadal time scales. *J. Phys. Oceanogr.,* **35,** 2090–2103.

Rossby, T., 1987: On the energetics of the Gulf Stream at 73°W. *J. Mar. Res.,* **45,** 59–82.

Shutts, G. J., 1986: A case study of eddy forcing during an atlantic blocking episode. *Anomalous Atmospheric Flows and Blocking,* B. Saltzman, B. Saltzman, and A. C. Wiin-Nielsen, Eds., Advances in Geophysics, Vol. 29, Adademic Press, 135–162.

Smith, K. S., and J. Marshall, 2009: Evidence for enhanced eddy mixing at middepth in the Southern Ocean. *J. Phys. Oceanogr.,* **39,** 50–69.

Smith, W. H. F., and D. T. Sandwell, 1997: Global seafloor topography from satellite altimetry and ship depth soundings. *Science,* **277,** 1957–1962.

Tracey, K. L., D. R. Watts, K. A. Donohue, and H. Ichikawa, 2012: Propagation of Kuroshio Extension meanders between 143°E and 149°E. *J. Phys. Oceanogr.,* **42,** 581–601.

Trenberth, K. E., and J. M. Caron, 2001: Estimates of meridional atmosphere and ocean heat transports. *J. Climate,* **14,** 3433–3443.

Tulloch, R., J. Marshall, C. Hill, and K. S. Smith, 2011: Scales, growth rates and spetral fluxes of baroclinic instability in the ocean. *J. Phys. Oceanogr.,* **41,** 1057–1076.

Volkov, D. L., T. Lee, and L.-L. Fu, 2008: Eddy-induced meridional heat transport in the ocean. *Geophys. Res. Lett.,* **35,** L06602, doi:10.1029/2008GL035490.

Walkden, G. J., K. J. Heywood, and D. P. Stevens, 2008: Eddy heat fluxes from direct measurements of the Antarctic Polar Front in Shag Rocks passage. *Geophys. Res. Lett.,* **35,** L06602, doi:10.1029/2007GL032767.

Waterman, S. N., and S. R. Jayne, 2011: Eddy–mean flow interactions in the along-stream development of a western boundary current jet: An idealized model study. *J. Phys. Oceanogr.,* **41,** 682–707.

——, ——, and N. G. Hogg, 2011: Eddy–mean flow interactions in the Kuroshio Extension region. *J. Phys. Oceanogr.,* **41,** 1182–1208.

Watts, D. R., X. Qian, and K. L. Tracey, 2001a: Mapping abyssal current and pressure fields under the meandering Gulf Stream. *J. Atmos. Oceanic Technol.,* **18,** 1052–1067.

——, C. Sun, and S. Rintoul, 2001b: A two-dimensional gravest empirical mode determined from hydrographic observations in the Subantartic Front. *J. Phys. Oceanogr.,* **31,** 2186–2209.

Wunsch, C., 1999: Where do ocean eddy heat fluxes matter? *J. Geophys. Res.,* **104** (C6), 13 235–13 249.